

Journal of Mechanics of Materials and Structures

**NUMERICAL SIMULATION OF FAILED ZONE PROPAGATION PROCESS
AND ANOMALIES RELATED TO THE RELEASED ENERGY DURING
A COMPRESSIVE JOG INTERSECTION**

Xue-Bin Wang, Jin Ma and Li-Qiang Liu

Volume 5, No. 6

June 2010



mathematical sciences publishers

NUMERICAL SIMULATION OF FAILED ZONE PROPAGATION PROCESS AND ANOMALIES RELATED TO THE RELEASED ENERGY DURING A COMPRESSIVE JOG INTERSECTION

XUE-BIN WANG, JIN MA AND LI-QIANG LIU

A compressive echelon fault structure is modeled using an explicit finite difference code (FLAC). The Weibull distribution is used to reflect the heterogeneity of elemental parameters. The released elastic strain energies due to shear and tensile failures are calculated using FISH functions. We examine the failed zone propagation process and the temporal and spatial distribution of the released strain energy, emphasizing those during the jog intersection.

A specimen including two parallel faults with an overlap is divided into square elements. Rock and faults are considered as nonhomogeneous materials with uncorrelated mechanical parameters (elastic modulus, tensile strength and cohesion). A Mohr–Coulomb criterion with tension cut-off and a post-peak brittle law are used. During the jog intersection, high values of released *tensile* strain energy are found at wing failure zones and at fault tips, while high values of released *shear* strain energy are found at faults. Despite the jog intersection, the released strain energy in the jog is not high.

We also introduce a quantity b_0 describing the slope of the curve connecting the number of failed elements and the energy released. This is similar to the quantity b found in the literature, but is expressed in units of J^{-1} . Before the jog intersection, some anomalies associated with shear sliding of rock blocks along faults can be observed from the number of failed elements (in shear, in tension and in either), the accumulated released strain energy due to shear and tensile failures, the strain energy release rates in shear and in tension, and the value of b_0 . As deformation proceeds, the evolution of b_0 is calculated according to two kinds of the released energy: total energy due to shear and tensile failures and shear strain energy. The two exhibit similar behavior, suggesting that the released strain energy in shear is much higher than in tension.

1. Introduction

Echelon fault structures can be observed in a wide range of length scales: they can be some 20 km long in the San Andreas fault [Segall and Pollard 1980], while in mining-induced normal faults observed in South Africa gold mines [Gay and Ortlepp 1979], echelon faults measured in centimeters can be found. The observed echelon cracks are even smaller in rock samples stressed in laboratory [Ewy and Cook 1990; Saimoto et al. 2003]. Seismologic evidence indicates that some earthquakes tend to cluster near echelon faults or in jogs [Segall and Pollard 1980; Sibson 1985]. Geologic evidence indicates that some basins and ranges can be formed in jogs [Aydin and Schultz 1990; Zachariassen and Sieh 1995]. Therefore, considerable attention has been given to the problems of deformation, failure process and stability of echelon fault structures [Bombolakis 1973; Segall and Pollard 1980; Sibson 1985; Ma et al. 1986; Aydin

Keywords: compressive echelon fault structure, jog intersection, failed zone, released strain energy, heterogeneity, shear failure.

and Schultz 1990; Du and Aydin 1991; Harris and Day 1993; Thomas and Pollard 1993; Zachariassen and Sieh 1995; Jiang et al. 2002; Chen et al. 2005; Ma et al. 2007; 2008; 2010].

Echelon fault structures fall into two categories, compressive and extensional, according to the stress state in the jog. For a compressive echelon fault structure, the jog is also called anti-dilatation or compressive, while for an extensional one, the jog is called a dilatation jog. Extensive evidence shows a marked difference between the two kinds, in stress distribution, secondary fracturing and magnitude of earthquakes [Segall and Pollard 1980; Sibson 1985; Aydin and Schultz 1990]. For a compressive echelon fault structure, the elastic interaction between two faults increases both the mean compressive stress between them and the frictional resistance at fault tips, inhibiting slip transfer across the jog. The compressive jog is a “pinned” area where much strain and strain energy can be stored [Segall and Pollard 1980; Sibson 1985; Ma et al. 2007; 2008; 2010]. Such a pinned jog is a potential nucleation site for moderate to large earthquakes. In contrast, in the extensional echelon fault structure, the frictional resistance at fault tips decreases, facilitating sliding [Segall and Pollard 1980; Sibson 1985]. For this reason, the present study is limited to compressive echelon structures.

Laboratory experiments, using transducers to measure displacement, strain, acoustic emissions (AE), and so on, have contributed greatly to ongoing research on faulting and rock failure, and have provided a vast amount of data, including waveforms, AEs and displacements on and around artificial faults [Paterson and Wong 2005]. Even with transducers, however, no accurate results are guaranteed. Narrow faults have been modeled physically by weak materials, such as gypsum mixture and wax paper [Shen et al. 1995]. It is often difficult to make precise direct measurements using transducers on and adjacent to faults. Therefore, energy accumulation and release are not clear in faults. Location errors in AE events may lead to inaccurate results — even that AE sources are located outside the sample boundaries [Lockner et al. 1991; Jiang et al. 2002]. For most experimental systems, insufficient AE data have been provided [Lei et al. 2000]. In addition, in AE tests, the released strain energy in shear and tensile failures cannot be distinguished from the total energy; and the individual sizes of failed zones in shear and in tension cannot be determined.

Stress and secondary fracturing distribution near jogs of two kinds of echelon fault structures were analyzed theoretically in [Segall and Pollard 1980]. A marked difference in behavior between them was found. However, this was a two-dimensional quasistatic study. In quasistatic analyses, some critical elements cannot be included, such as stress waves and time-dependent stress concentrations [Harris and Day 1993]. Therefore, dynamic rupture propagation analyses were advocated by Harris and Day. However, their model is purely elastic, in which the rupture cannot break through into the rock medium surrounding faults.

The studies mentioned mainly focus on the interaction between faults and the distribution of stress and displacement. The following problems are left untouched: the temporal and spatial distribution of the released elastic strain energy during the jog intersection and the corresponding change in macroscopic mechanical behavior, precursors to the jog intersection or the consequent unstable sliding of rock blocks along faults and the relation between the number of events and the released energy.

The principal objective of this paper is to examine these problems numerically by use of FLAC (“Fast Lagrangian Analysis of Continua”), an explicit finite-difference code that can be used to model geologic structures [Strayer and Hudleston 1997; McKinnon and de la Barra 1998; Erickson et al. 2001], rock specimens with imperfections and joints, [Wang 2005; Wang 2007a; Wang 2007b; Wang 2007c; Wang

2008; Wang et al. 2009] and heterogeneous rock specimens [Cundall 1989; Fang and Harrison 2002; Wang and Pan 2008; Wang and Zhang 2009].

2. Introduction of heterogeneity and calculation of released energy

Weibull's theory is known to be useful for tensile fractures. There are still arguments on whether it is also appropriate for fracturing in compression [Paterson and Wong 2005]. For brittle materials, the Weibull distribution function has been used in considering the distribution of microdefects [Tang and Kou 1998; Liu et al. 2004]. Here it is still used to describe the heterogeneity in an elemental parameter:

$$f(u) = \frac{m}{u_0} \left(\frac{u}{u_0}\right)^{m-1} \exp\left(-\left(\frac{u}{u_0}\right)^m\right) \quad (1)$$

where u is the elemental parameter, with mean u_0 , and m is the shape parameter describing the scatter of u . Higher values of m mean the material is more homogeneous.

FLAC includes a programming language, FISH, which allows the definition of new functions, thus providing great flexibility. In [Wang 2007b; 2008; Wang et al. 2009] we used FISH functions to introduce random material imperfections with the same strength within rock specimens. A similar method is used in the present paper to consider the heterogeneity in an elemental parameter satisfying the statistical distribution above.

If an element undergoes shear or tensile failure, the stored elastic strain energy is given by

$$W = \frac{V}{2E} (\sigma_1^2 + \sigma_2^2 + \sigma_3^2 - 2\nu(\sigma_1\sigma_2 + \sigma_1\sigma_3 + \sigma_2\sigma_3)), \quad (2)$$

where E is the elastic modulus, σ_1 , σ_2 and σ_3 are the principal stresses, ν is the Poisson's ratio and V is the volume of the element.

This equation is applied as follows. Once an element is found to fail in shear, the value given by the formula is the stored shear strain energy, and likewise for an element undergoing tensile failure. Equation (2) is applied once every 10 timesteps. Once the stored shear or tensile strain energy for an element is found to decrease, the change in the energy is remembered for the element. This part of the energy is the released elastic strain energy in shear or in tension. In any 10 timesteps, summing the released elastic strain energy of all elements leads to the elastic strain energy release rate whose units are still J . Then, for the time interval of interest (from a beginning to an ending timestep), we sum the elastic strain energy release rate to obtain the accumulated released elastic strain energy.

We next introduce a quantity we call b_0 , which is the negative of the slope of the line relating the log of the number of failed elements and the released energy. Here is how b_0 is calculated. In a given timestep interval, the element releasing the maximum elastic strain energy E_{\max} is found among all elements. We find that the elements releasing higher strain energy are fewer than those releasing lower energy. If all data about energy are used to obtain the relation between the number of failed elements and the released elastic strain energy, then possibly the relation is not monotonic. Therefore, a part of the data may need to be omitted. For this we introduce two factors: the cut-off factor P and the classification factor Q (Figure 1). All data higher than $E_0 = E_{\max} \cdot P$ are discarded. The remaining energy interval, from 0 to E_0 , is divided into Q subintervals. The calculation of b_0 is made from the residual data sorted according to subinterval. For each subinterval, the average released average strain energy can be calculated according

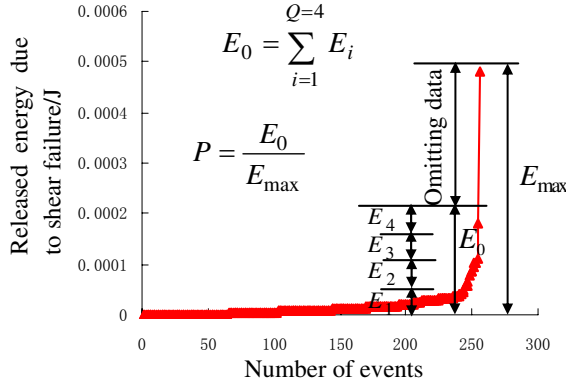


Figure 1. Definitions of the cut-off factor and classification factor.

to the upper and lower limits of the released energy. The number of failed elements in each level and its logarithm need to be determined. For each level, the same operation is executed. Thus, the relation between the logarithm of the number and the average released energy can be determined. Linearly fitting the relation and multiplying the slope by -1 yields b_0 , whose units are J^{-1} , different from the common b -value [Lockner et al. 1991; Main et al. 1992; Sammonds et al. 1992; Lei et al. 2000].

3. Numerical model and constitutive parameters

3.1. Constitutive models. For elements in elastic stage, an isotropic model is used:

$$\Delta\sigma_{ij} = 2G\Delta\epsilon_{ij} + \left(K - \frac{2}{3}G\right)\Delta\epsilon_{kk}\delta_{ij} \quad (3)$$

where $\Delta\sigma_{ij}$ is the stress tensor, $\Delta\epsilon_{ij}$ is the strain tensor, G is the shear modulus, K is the bulk modulus and δ_{ij} is the Kronecker sign. G and K are related to two elastic parameters: elastic modulus and Poisson's ratio.

As is known, the Mohr–Coulomb criterion can overestimate the tensile strength of brittle materials. Therefore, a tension cut-off is needed. For the Mohr–Coulomb criterion with tension cut-off, the initial yield function includes two parts: the shear yield function

$$f^s = \sigma_1 - \sigma_3 N_\phi + 2c\sqrt{N_\phi} = 0, \quad (4)$$

depending on the the initial cohesion c and the initial internal friction angle ϕ , via $N_\phi = \frac{1 + \sin \phi}{1 - \sin \phi}$, and the tensile yield function

$$f^t = \sigma_3 - \sigma_t = 0, \quad (5)$$

depending on the initial tensile strength σ_t .

Accordingly, the plastic potential function governing plastic flows is composed of two parts: the shear potential function

$$g^s = \sigma_1 - \sigma_3 N_\psi \quad (6)$$

and the tensile potential function

$$g^t = \sigma_3. \quad (7)$$

In (6), ψ is the dilatation angle; the functional dependence of N_ψ on ψ is the same as that of N_ϕ on ϕ .

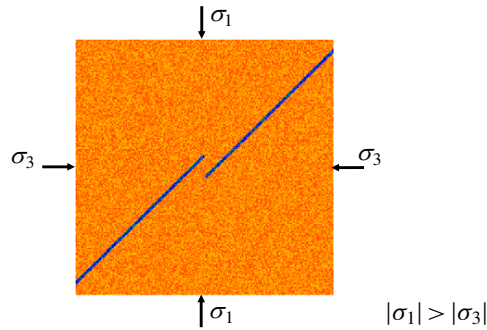


Figure 2. Computational model for the compressive echelon fault structure.

Once an element fails as deformation proceeds, the stress state will not reside on the initial yield surface and will drop to the yield surfaces determined by the present cohesion, internal friction angle and tensile strength. These yield surfaces lie below the initial yield surface. Eventually, as deformation proceeds, the stress state will stop on the residual yield surface controlled by the residual strength parameters.

3.2. Computational model and parameters. Figure 2 shows the computational model of a specimen whose size is $0.3 \text{ m} \times 0.3 \text{ m}$. The specimen is composed of a rock block and two faults. Two faults form an echelon fault structure, which are oriented at 45° from the horizontal direction. The fault overlap is equal to the distance between two faults, i.e., $1.84 \times 10^{-2} \text{ m}$. The specimen is divided into 300×300 elements and faults are composed of 1.493×10^3 elements. Elements in faults are determined through their centroid coordinates by use of a written FISH function for identifying a joint in rock specimens [Wang 2005; 2007a]. The present numerical model represents a plane strain problem and only a small strain mode is permitted.

Two steps of calculation are carried out. In the first step, a hydrostatic pressure of 2 MPa is applied to four specimen boundaries. This step consumes 2×10^4 timesteps. A timestep (or step, computational step) in FLAC is a cycle in which constitutive equations for elements and equations of motion for gridpoints or nodes are executed one time. Large complex problem can require tens of thousands of timesteps to reach a steady state. During computation stepping, information is propagated across the elements in the finite difference grid. After calculating 2×10^4 cycles, the maximum unbalanced force among nodes has been found to be small enough, and the specimen is considered to have reached a static equilibrium state. In FLAC, each gridpoint is surrounded by elements that contribute forces to the gridpoint. At equilibrium, the algebraic sum of these forces is almost zero. When failure and plastic flow are occurring within a model, the unbalanced force of some nodes can be nonzero, among which the maximum value is usually called the maximum unbalanced force that can be displayed in FLAC. It is a good tool for assessing the state of a model, such as equilibrium or plastic flow.

In the second step, a displacement-controlled loading is conducted in the vertical direction (σ_1 direction in Figure 2 in which $\sigma_3 = 2 \text{ MPa}$) with a small compressive velocity of $v = 1 \times 10^{-9} \text{ m/timestep}$. According to the stress state in the jog, the echelon fault structure belongs to a compressive one.

In this paper, three mechanical parameters (elastic modulus, initial cohesion and initial tensile strength) are declared to obey the Weibull distribution, and a value of $m = 9$ is used. The three parameters are *a priori* uncorrelated. This suggests that for an element, if its initial cohesion is higher, then its elastic

modulus or initial tensile strength is possibly lower. The point of assigning uncorrelated parameters is to increase the complexity of elemental mechanical parameters with position variation.

The reported values of Poisson's ratio for marble and gypsum are 0.25 and 0.2, respectively [Chen et al. 2005]. These values are used in the isotropic elastic model. The reported values of elastic modulus for marble and gypsum are 55 GPa and 5.1 GPa, respectively [Chen et al. 2005]. These values are adopted as average values in the isotropic elastic model. For rock and fault elements, average values of initial cohesion are assumed to be 37.5 MPa and 5 MPa, respectively; average values of initial tensile strength are 12 MPa and 1.2 MPa, respectively; initial internal friction angles are 50° and 10° , respectively. The dilatation angle is 0° for two kinds of materials.

In fact, for most rock materials, the post-peak behavior exhibits apparent brittle nature at low confining pressures [Wawersik and Fairhurst 1970]. Once elements fail, they are assumed to undergo a linear strain-softening behavior followed by a residual deformation stage. For both kinds of elements, we assume that the residual strength will be reached immediately after failures occur. This means that the plastic strain corresponding to the beginning of the residual deformation stage is extremely low. In the present paper, the values of residual tensile strength and cohesion of rock elements are assumed to be zero. When the plastic strain exceeds 5×10^{-6} (an extremely low value to reflect the brittle nature of rock elements), it is assumed that rock element completely loses its cohesion and tensile strength. For fault elements, the values for residual tensile strength and cohesion are assumed to be zero. When the plastic strain is larger than 5×10^{-7} (0.1 times the value for rock elements), it is assumed that fault elements have completely lost their cohesion and tensile strength. For rock and fault elements, a small residual internal friction angle of 1° is used to model the relative weak fault gouge and to create an obvious response in the macroscopic mechanical behavior (stress-timestep curve) during the jog intersection.

4. Results and discussion

4.1. Stress-timestep curve and propagation process of failed zones. Figure 3 shows the stress-timestep curve of the specimen including a compressive jog and the relation between the maximum unbalanced force and the timestep. The stress-timestep curve is basically the same as the stress-strain curve. The

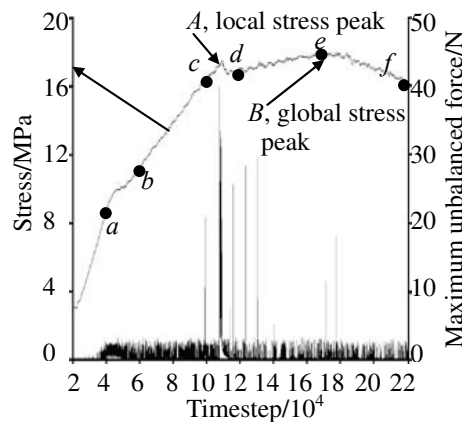


Figure 3. Stress-timestep curve and maximum unbalanced force-timestep curve.

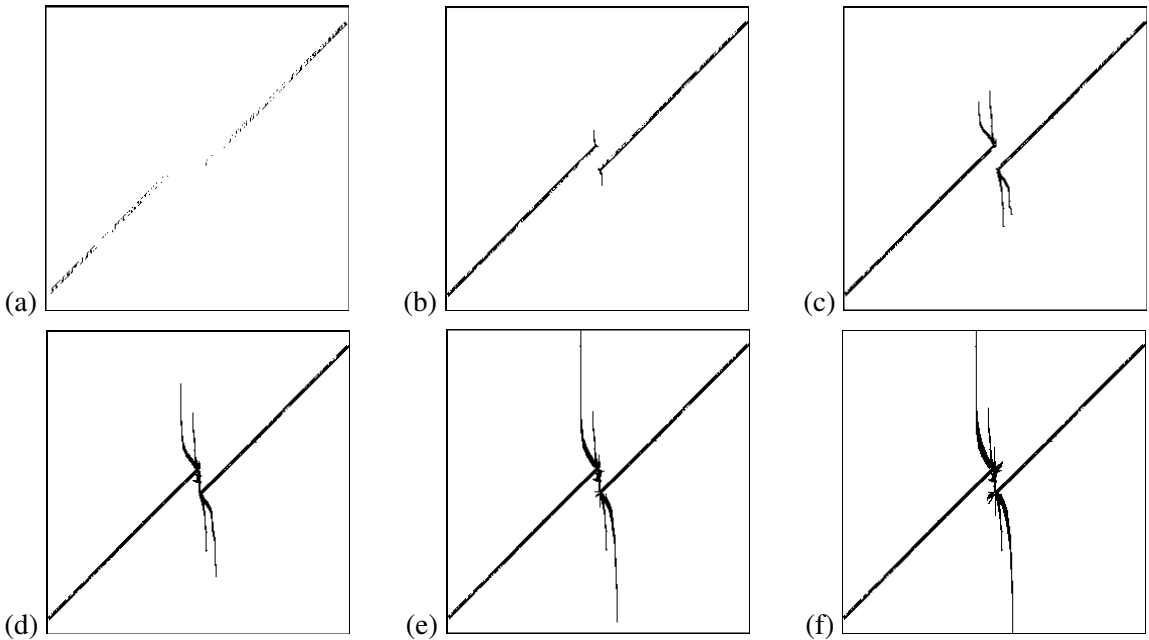


Figure 4. Failure patterns at different timesteps: (a) = 4×10^4 , (b) = 6×10^4 , (c) = 1×10^5 , (d) = 1.2×10^5 , (e) = 1.7×10^5 , (f) = 2.2×10^5 .

formula $\epsilon_a = vt/L$ can be used to convert ϵ_a (axial strain) from t (timestep) and L (height of the specimen). Figure 4 shows the failure process of the echelon fault structure. Black elements are failed elements. The stress-timestep curve can be roughly divided into four stages based on its slope.

Let's consider Figure 4 in light of the stress-timestep graph in Figure 3. Points a – f in the latter correspond to parts (a)–(f) of the former. In the first stage, the stress-timestep graph has a fairly high slope, and is relatively smooth and straight. In this stage, the failed elements are at the faults — see Figure 4(a) — due to the weakness of faults.

In the second stage, the graph becomes less smooth and its slope decreases. At this stage, failed zones extend outwards from the fault tips. In Figure 4(b), there are two failed zones pointing up and down, while in Figure 4(c), the two failed zones become even longer and two wing failure zones also extend outwards from two fault tips. Cracks formed toward the outside of the jog can be observed in tests [Jiang et al. 2002; Chen et al. 2005; Ma et al. 2008], in steeply dipping-mining-induced normal faults in South Africa [Gay and Ortlepp 1979] and in granitic rocks of the Sierra Nevada [Segall and Pollard 1980]. Based on the elastic model, tensile cracks are formed at fault tips and propagate outwards [Segall and Pollard 1980]. The present numerical results agree with these observations and theoretical results.

In the third stage, a local stress peak is formed (point A in Figure 3) and the jog is intersected by elements arranged in a vertical direction. After that, the stress increases slightly in a long timestep interval until a global stress peak is reached (point B in Figure 3). Failed zones outside the jog become even longer. We see in Figure 4(d,e) that the vertical failure zones have stopped, while the wing failure zones continuously extend toward loading ends of the specimen. In Figure 4(e), they have reached the loading ends.

In the fourth stage, the load-carrying capacity of the specimen is slowly decreased and the specimen will collapse. The failure patterns of the specimen do not change; see Figure 4(f).

It is noted that the vertical failure zones outside the jog stop during the propagation of wing failure zones. The reason will be discussed in the next section.

4.2. Intersection process of the jog. Figure 5 shows the propagation of failed zones in the jog intersection process: black elements have failed in shear or in tension, while the scale of yellows and reds represents the magnitude of tensile strength for an unfailed element (redder or darker = higher tensile strength). Figure 6 shows the corresponding timesteps as points *a*, *b*, *c*, *d*. Thus, Figure 5(c) corresponds to the local stress peak (point A in Figure 3). Parts (a) and (b) of Figure 5 represent the situation pre-peak, while part (d) is post-peak.

It is found from Figure 5(a) that wing failure zones are more curved near fault tips, which are perpendicular to faults. They tend to grow in the vertical direction with an increase of their length, parallel to the vertical failure zones. These two kinds of failed zones nearly have the same distance from their tips to loading ends. In part (a) of the figure, the jog has not been bisected and the maximum unbalanced force among nodes is low. In part (b), the jog is bisected and tips of wing failure zones have exceeded those of the vertical failure zones. At about 1.0745×10^5 timesteps (Figure 6), the maximum unbalanced

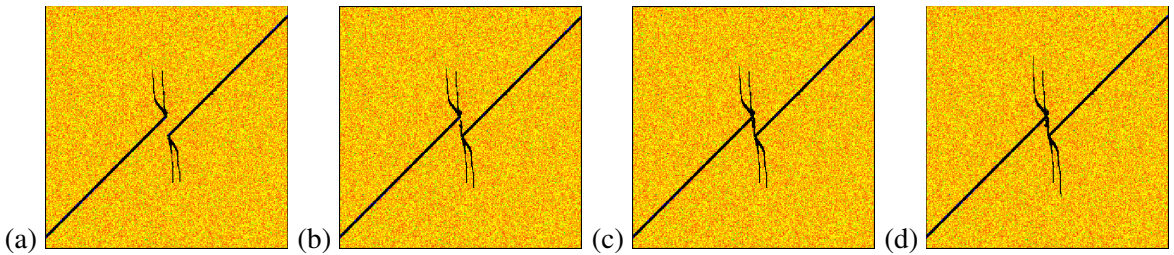


Figure 5. Jog intersection process at different timesteps: (a) = 1.06×10^5 , (b) = 1.08×10^5 , (c) = 1.09×10^5 , (d) = 1.12×10^5 .

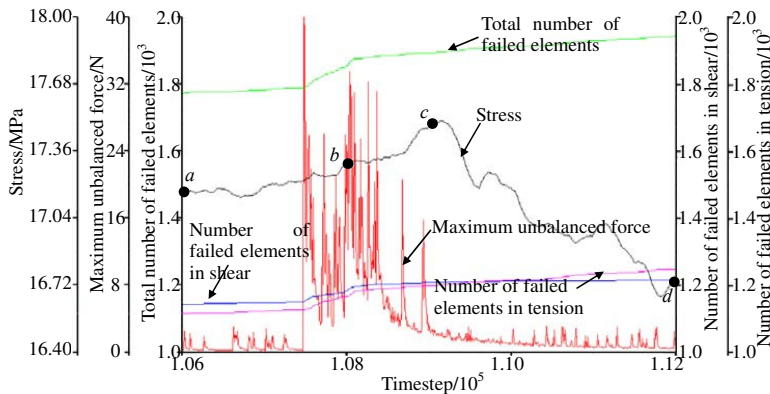


Figure 6. Evolution of stress, maximum unbalanced force, and number of failed elements (in shear, in tension, and in either) during the jog intersection. Note clipped vertical scales. For the horizontal scale, 10^5 timesteps equal axial strains of 3.33×10^{-4} .

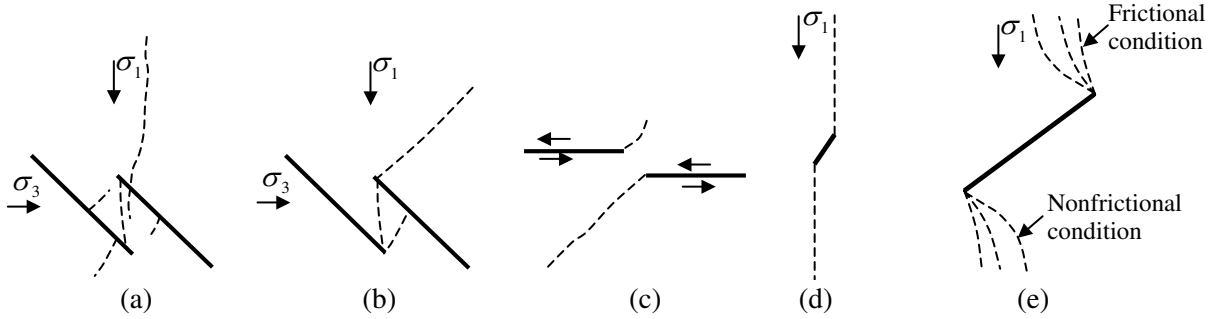


Figure 7. Observed cracks extending outwards and inwards from fault tips (a,c) and some straight and wing cracks (d,e). Part (a) from [Jiang et al. 2002], (b) from [Chen et al. 2005], (c) from [Segall and Pollard 1980], (d) from [Ewy and Cook 1990], (e) from [Shen et al. 1995].

force begins to increase rapidly. This phenomenon ends at about 1.084×10^5 timesteps. During the rapid increase in the maximum unbalanced force, the jog is bisected. In parts (c) and (d) of Figure 5, the wing failure zones become even longer. Beyond timesteps of 1.084×10^5 , the maximum unbalanced force exhibits a decreasing tendency. However, there are two major peaks (at 1.09×10^5 and 1.093×10^5 timesteps) in the maximum unbalanced force; beyond the local stress peak, many minor peaks can be observed.

Parts (a)–(c) of Figure 7 show experimental failure modes of compressive echelon fault structures [Jiang et al. 2002; Chen et al. 2005] and field observation [Segall and Pollard 1980]. Two kinds of cracks (dotted lines) can be found: cracks extending outwards, not linking faults, and those linking fault tips. These observed cracks are similar in geometry to those in the present numerical study results. The vertical failure zones outside the jog, which are observed in the present numerical results, are especially similar to splitting cracks from a slip interface in the simplified model of [Ewy and Cook 1990]; see Figure 7(d). Wing fractures originating from a preexisting fracture were also observed in many experiments [Horii and Nemat-Nasser 1985; Shen et al. 1995; Dyskin et al. 1999; Saimoto et al. 2003]. Using a displacement discontinuous method, Shen and Stephansson found that a stiff contact condition (high normal fracture stiffness and high shear fracture stiffness) produces straight wing fractures similar to the present vertical failure zones, while a noncontact condition (zero normal fracture stiffness and zero shear fracture stiffness) leads to curved wing fractures analogous to the present wing failure zones. Both types are shown in Figure 7(e).

It is found from the present numerical results that the vertical failure zones stop when their length reach a critical value. After wing failure zones appear, they extend continuously. This phenomenon may be due to the change in the internal friction angle of the faults beyond failure: when elements in faults just fail, their internal friction angles are high, but when elements in faults enter the residual deformational stage, lower internal frictional angles are expected. Following [Shen et al. 1995], we can say that in the first case the fault is similar to a frictional fracture, resulting in straight failed zones, while in the second case, the behavior of the fault is equivalent to that of a nonfrictional fracture, thus inducing curved wing failure zones.

4.3. Temporal and spatial distribution of the released energy in the jog intersection process. Figure 8 shows the temporal and spatial distribution of the released elastic strain energy before the jog intersection and beyond. Green color regions denote faults. The radii of black and red circles denote magnitudes of the released shear and tensile strain energy, respectively. The four images at the bottom are close-ups of the four at the top, emphasizing the jog. The markers *a–d* in Figure 6 correspond to (a)–(d) and (aa)–(dd) in Figure 8.

It is found from (a) and (aa) that the released shear strain energy is high at faults, while the released tensile strain energy is high at fault tips. Parts (b) and (bb) reveal that, after the jog intersection, failed zones linking fault tips in the jog liberate both strain energy in shear and in tension. The latter is lower.

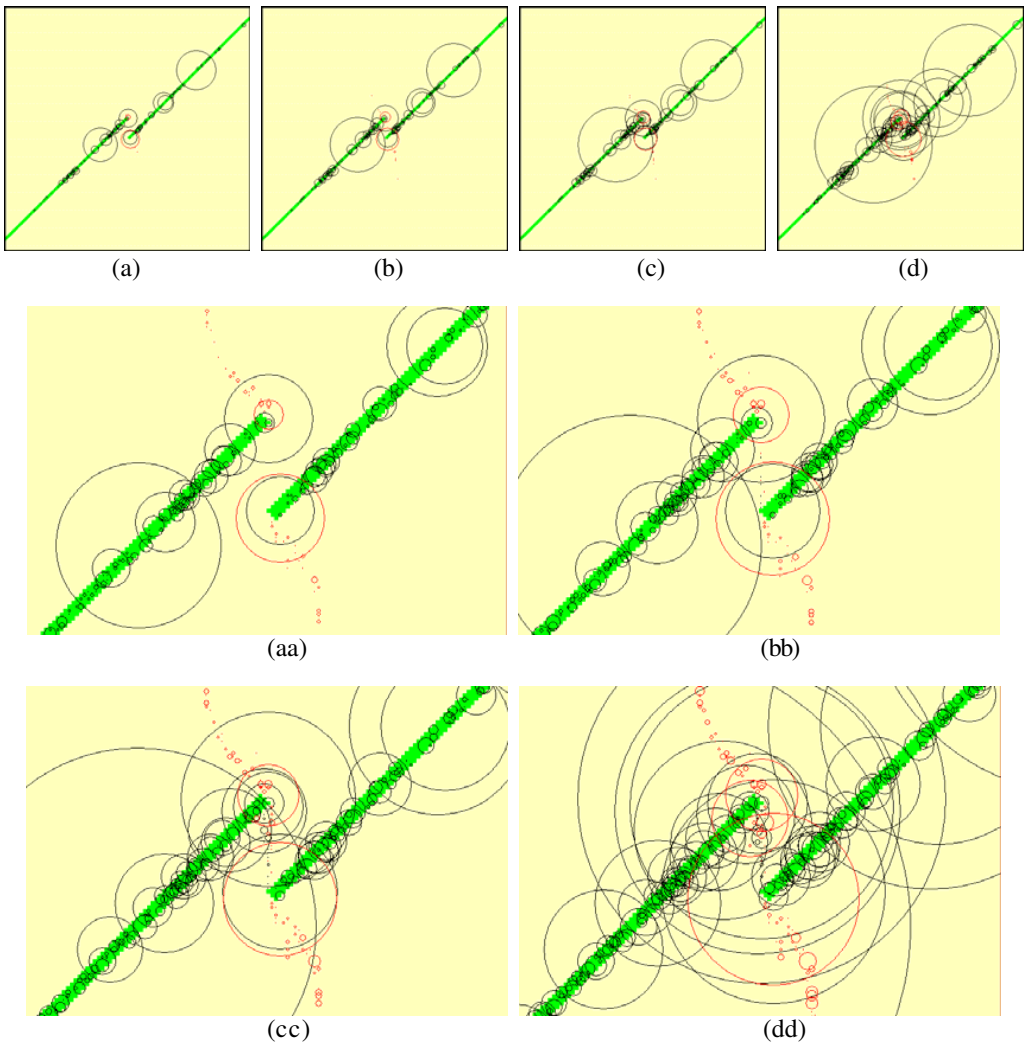


Figure 8. Spatial and temporal distribution of the liberated energy in the jog intersection process. Timesteps are 1.06×10^5 for (a) and (aa), 1.08×10^5 for (b) and (bb), 1.09×10^5 for (c) and (cc), and 1.12×10^5 for (d) and (dd).

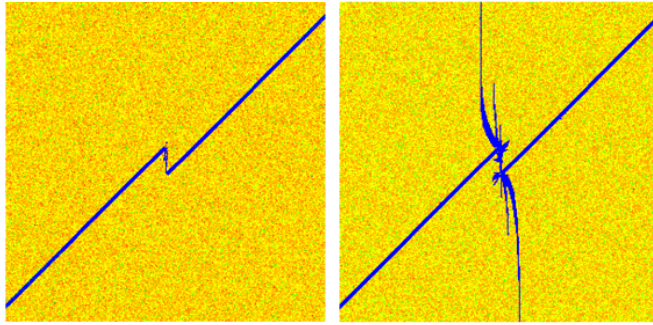


Figure 9. Failed zones in shear (left) and in tension (right).

The remaining images suggest that in the strain-softening stage beyond the local stress peak, many sites in faults release a great deal of elastic strain energy, implying occurrence of many events associated with abrupt shear sliding of rock blocks along faults.

Note that a relatively small amount of strain energy is released in the vertical failure zones in the jog and outside, while a large amount is liberated in wing failure zones and at fault tips. Much strain energy in shear is released at faults, especially at their tips.

4.4. Evolution of the number of failed elements. Figure 9 shows the location of failed elements (blue) at 2.2×10^5 timesteps. The figure reveals that shear and tension failures occur at faults, also in the vertical failed zone in the jog. Failures in the vertical failure zones outside the jog and in wing failure zones are due to tension. The elastic model predicts that antithetic shear fractures bisect the jog [Segall and Pollard 1980], which is consistent with the present numerical results. However, the jog is subjected to both shear and tensile failures in the present simulation.

In Figure 6 we showed the evolution of the number of failed elements. (Since some elements fail both in shear and in tension, the topmost curve, showing the number of failed elements in either shear or tension, does not equal the sum of the two lowest curves, showing the number of elements failing in each mode.)

To better clarify this evolution, the figure also shows stress and maximum unbalanced force as function of timestep. One sees that before the maximum unbalanced force begins to increase rapidly (at about 1.0745×10^5 timesteps) the numbers of failed elements (in shear, in tension, or in either) increase steadily. During the rapid increase in the maximum unbalanced force, these numbers increase rapidly. These phenomena occur prior to the local stress peak. Beyond the peak, there is little change in the number of failed elements in shear, while the other two numbers continue to increase significantly. The reason for this is the extending wing failure zones where tensile failure propagates continuously beyond the jog intersection.

4.5. Evolution of the accumulated released energy and the energy release rate. The top graph in Figure 10 shows the evolution of the released energy due to shear failure and the energy release rate in shear (i.e., the released energy due to shear failure per 10 timesteps, whose units are still J). As can be seen from the figure, before the maximum unbalanced force rapidly increases (at about 1.0745×10^5 timesteps), the released energy in shear increases linearly. Afterwards, the released shear strain energy-timestep

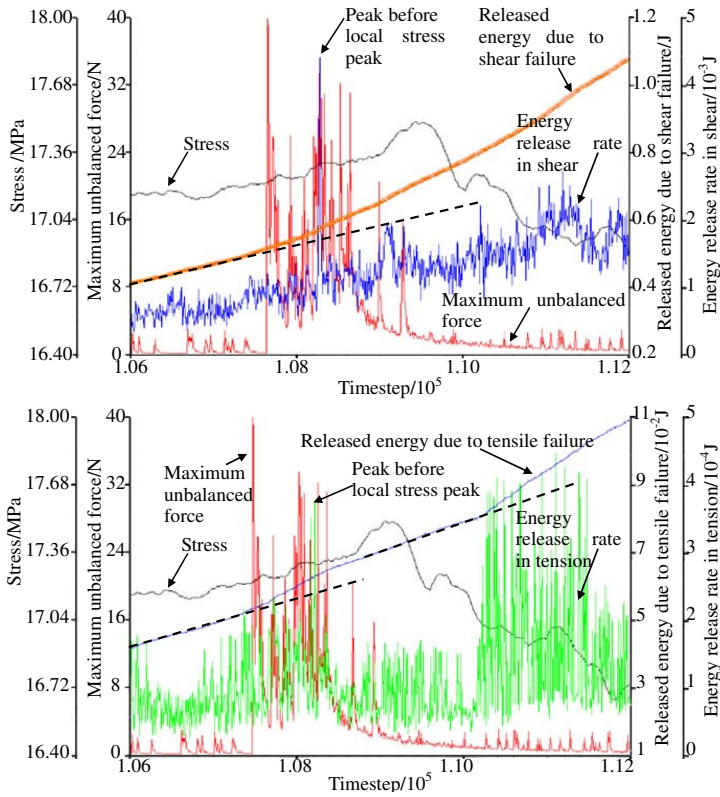


Figure 10. Evolution of the released strain energy and the strain energy release rate with timestep during the jog intersection for the case of shear strain energy (top) and tensile strain energy (bottom).

curve exhibits an apparent change in slope, deviating from the dotted line. (In fact some deviation from linearity occurs even prior to the local stress peak: the curve exhibits a concave-upward behavior.)

The energy release rate in shear is relatively low before the rapid increase in the maximum unbalanced force and the fluctuating amplitude is also low. Next, a peak of the energy release rate is formed. Afterwards, although the energy release rate in shear is lower than the peak, it is higher than before the rapid increase in the maximum unbalanced force. Moreover, the fluctuation is more obvious.

The bottom graph in [Figure 10](#) shows the evolution of the released energy due to tensile failure and the energy release rate in tension. Two apparent slope changes occur in the released energy in tension (the dotted lines show the slope before each change). The first change corresponds to the rapid increase in the maximum unbalanced force, in which a high energy release rate in tension can be observed. This change is caused by a large amount of energy release in tension due to the jog intersection. The second change begins at about 1.102×10^5 timesteps, and is due to extension of wing failure zones. The energy release rate in tension is higher and fluctuates greatly.

4.6. Evolution of b_0 using two kinds of energy. Eighty timestep intervals, each 500 timesteps long, are taken covering the range from timestep 8.75×10^4 to 1.275×10^5 . The value of b_0 for each interval

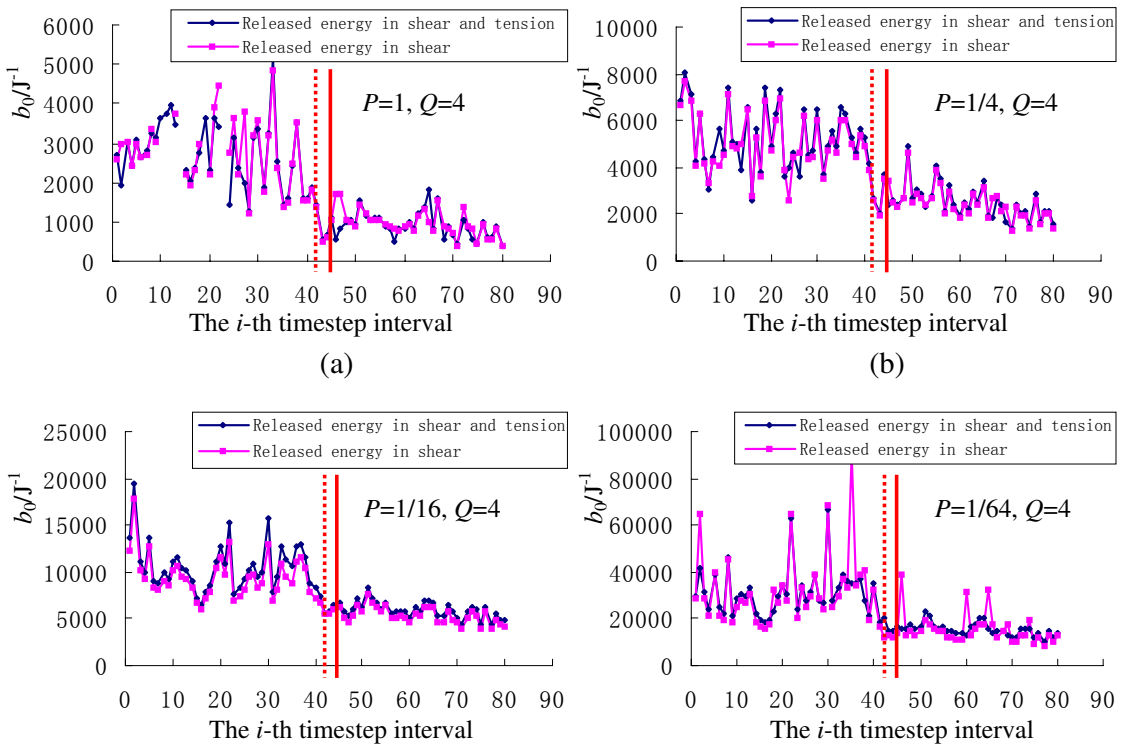


Figure 11. Evolution of b_0 according to the released energy due to shear failure and the released energy due to shear and tensile failures from 87500 to 127500 timesteps at different cut-off factors P . The dotted vertical line denotes the jog intersection and the solid one corresponds to the local stress peak.

is calculated as described on page 1009 and plotted in Figure 11. At the 41st interval (dotted vertical line), the jog is intersected. Local stress peak appears in the 44th interval (solid line). Figure 11 shows the evolution of b_0 according to two kinds of the released energy: energy due to failures and that solely due to tensile failure. These results reveal that b_0 fluctuates at a higher level and then decreases to a lower level. Transition between the two levels can be found at timestep roughly corresponding to the local stress peak. For a low cut-off factor P (omitting many big data), the fluctuation in b_0 is apparent. Experimental results show that the related variable b decreases to a single minimum or double minimum before fault nucleation [Lockner et al. 1991; Lei et al. 2000] and before rapid stress drop [Main et al. 1992; Sammonds et al. 1992]. The present numerical results support these findings. However, the recovery for b_0 from the minimum cannot be observed in Figure 11.

Only a small difference exists in b_0 according to two kinds of energy. This suggests that the released energy due to shear failure is much higher than that due to tensile failure. For the sake of simplicity of calculation, seemingly, the released energy in shear is sufficient in calculating the evolution of b_0 . No value for b_0 is calculated in some timestep intervals in Figure 11(a) since big events are greater and small events are fewer, leading to a nonmonotonic relation between the log of the number of failed elements and the released elastic strain energy. Therefore, an appropriate selection of the cut-off factor P is necessary.

5. Conclusions

Two kinds of failed zones initiated from fault tips are observed in the process of the compressive jog intersection. The vertical failed zones outside the jog occur earlier and then stop. The wing failure zones appear later and then extend continuously toward the outside of the jog. The possible reason for this phenomenon stems from the decreasing internal friction angle of faults at post-peak. During the jog intersection, high released tensile strain energy is found at wing failure zones and at fault tips, while high released shear strain energy is at faults. Despite the jog intersection, the released strain energy in the jog is not high. After the jog intersection, a local stress peak is reached and then much shear strain energy is released at faults, indicating that a number of events related to abrupt shear sliding of rock blocks along faults occur.

Before the jog intersection, some anomalies associated with shear sliding of rock blocks along faults can be observed: rapid increases in the numbers of failed elements in shear and in tension, rapid increases in the accumulated strain energy released due to shear and tensile failures, peak values of strain energy release rates in shear and in tension, and b_0 -value transition from higher values with higher fluctuating amplitude to lower values with lower fluctuating amplitude. As deformation proceeds, the evolution of b_0 is calculated according to two kinds of energy exhibits similar behavior. This suggests that the released strain energy in shear is much higher than that in tension, facilitating the calculation of b_0 with timestep or exerted strain in the displacement-controlled direction.

Acknowledgements

We are grateful to an anonymous reviewer for his helpful comments and suggestions in improving the manuscript. This work was supported by the National Natural Science Foundation of China (50974069) and the open research fund (LED2010B04) of State Key Laboratory of Earthquake Dynamics, Institute of Geology, China Earthquake Administration.

References

- [Aydin and Schultz 1990] A. Aydin and R. A. Schultz, “Effect of mechanical interaction on the development of strike-slip faults with echelon patterns”, *J. Struct. Geol.* **12**:1 (1990), 123–129.
- [Bombolakis 1973] E. G. Bombolakis, “Study of the brittle fracture process under uniaxial compression”, *Tectonophys.* **18**:3–4 (1973), 231–248.
- [Chen et al. 2005] J.-D. Chen, S.-P. Ma, S.-J. Liu, and G.-C. Jin, “An experimental study of the failure process of en-echelon fault structure using the digital speckle correlation method”, *Chin. J. Geophys.* **48**:6 (2005), 1350–1356. In Chinese.
- [Cundall 1989] P. A. Cundall, “Numerical experiments on localization in frictional materials”, *Ing. Arch.* **59**:2 (1989), 148–159.
- [Du and Aydin 1991] Y. Du and A. Aydin, “Interaction of multiple cracks and formation of echelon crack arrays”, *Int. J. Numer. Anal. Methods Geomech.* **15**:3 (1991), 205–218.
- [Dyskin et al. 1999] A. V. Dyskin, L. N. Germanovich, and K. B. Ustinov, “A 3-D model of wing crack growth and interaction”, *Eng. Fract. Mech.* **63**:1 (1999), 81–110.
- [Erickson et al. 2001] S. G. Erickson, L. M. Strayer, and J. Suppe, “Initiation and reactivation of faults during movement over a thrust-fault ramp: numerical mechanical models”, *J. Struct. Geol.* **23**:1 (2001), 11–23.
- [Ewy and Cook 1990] R. T. Ewy and N. G. W. Cook, “Deformation and fracture around cylindrical openings in rock, II: initiation, growth and interaction of fractures”, *Int. J. Rock Mech. Min.* **27**:5 (1990), 409–427.
- [Fang and Harrison 2002] Z. Fang and J. P. Harrison, “Development of a local degradation approach to the modelling of brittle fracture in heterogeneous rocks”, *Int. J. Rock Mech. Min.* **39**:4 (2002), 443–457.

- [Gay and Ortlepp 1979] N. C. Gay and W. D. Ortlepp, “Anatomy of a mining-induced fault zone”, *Geol. Soc. Am. Bull.* **90**:1 (1979), 47–58.
- [Harris and Day 1993] R. A. Harris and S. M. Day, “Dynamic of fault interaction: parallel strike-slip faults”, *J. Geophys. Res.* **98**:B3 (1993), 4461–4472.
- [Horii and Nemat-Nasser 1985] H. Horii and S. Nemat-Nasser, “Compression-induced microcrack growth in brittle solids: axial splitting and shear failure”, *J. Geophys. Res.* **90**:B4 (1985), 3105–3125.
- [Jiang et al. 2002] H.-K. Jiang, S.-L. Ma, L. Zhang, H.-F. Hou, and W.-H. Cao, “Spatio-temporal characteristics of acoustic emission during the deformation of rock samples with compressional and extensional en-echelon fault pattern”, *Acta Seismol. Sin.* **4** (2002), 385–396. In Chinese; translated in *Acta. Seismol. Sin.* **15**:4 (2002), 402–413.
- [Lei et al. 2000] X. Lei, K. Kusunose, M. V. M. S. Rao, O. Nishizawa, and T. Satoh, “Quasi-static fault growth and cracking in homogeneous brittle rock under triaxial compression using acoustic emission monitoring”, *J. Geophys. Res.* **105**:B3 (2000), 6127–6139.
- [Liu et al. 2004] H. Y. Liu, S. Q. Kou, P.-A. Lindqvist, and C. A. Tang, “Numerical studies on the failure process and associated microseismicity in rock under triaxial compression”, *Tectonophys.* **384**:1–4 (2004), 149–174.
- [Lockner et al. 1991] D. A. Lockner, J. D. Byerlee, V. Kukusenko, A. Ponomarev, and A. Sidorin, “Quasi-static fault growth and shear fracture energy in granite”, *Nature* **350** (1991), 39–42.
- [Ma et al. 1986] J. Ma, Y. Du, and L. Liu, “The instability of en-echelon cracks and its precursors”, *J. Phys. Earth* **34** (1986), S141–S157.
- [Ma et al. 2007] J. Ma, L.-Q. Liu, P.-X. Liu, and S.-L. Ma, “Thermal precursory pattern of fault unstable sliding: an experimental study of en echelon faults”, *Chin. J. Geophys.* **50**:4 (2007), 1141–1149. In Chinese.
- [Ma et al. 2008] S. L. Ma, S. Y. Chen, P. X. Liu, X. Y. Hu, K. Y. Wang, and Y. M. Huang, “Effect of fault jogs on frictional behavior: an experimental study”, *Sci. Chin. D* **51**:10 (2008), 1436–1445.
- [Ma et al. 2010] J. Ma, S. P. Ma, L. Liu, and P. X. Liu, “Experimental study of thermal and strain fields during deformation of en echelon faults and its geological implications”, *Geodyn. Tectonophys.* **1**:1 (2010), 24–35.
- [Main et al. 1992] I. G. Main, P. G. Meredith, and P. R. Sammonds, “Temporal variations in seismic event rate and *b*-values from stress corrosion constitutive laws”, *Tectonophys.* **211**:1–4 (1992), 233–246.
- [McKinnon and de la Barra 1998] S. D. McKinnon and I. G. de la Barra, “Fracture initiation, growth and effect on stress field: a numerical investigation”, *J. Struct. Geol.* **20**:12 (1998), 1673–1689.
- [Paterson and Wong 2005] M. S. Paterson and T.-F. Wong, *Experimental rock deformation: the brittle field*, 2nd ed., Springer, Berlin, 2005.
- [Saimoto et al. 2003] A. Saimoto, Y. Imai, and T. Hashida, “The genesis of echelon-mode-I cracks in the neighbourhood of a mode-II-crack tip under uniaxial compression”, *Key Eng. Mater.* **251–252** (2003), 327–332.
- [Sammonds et al. 1992] P. R. Sammonds, P. G. Meredith, and I. G. Main, “Role of pore fluids in the generation of seismic precursors to shear fracture”, *Nature* **359** (1992), 228–230.
- [Segall and Pollard 1980] P. Segall and D. D. Pollard, “Mechanics of discontinuous faults”, *J. Geophys. Res.* **85**:B8 (1980), 4337–4350.
- [Shen et al. 1995] B. Shen, O. Stephansson, H. H. Einstein, and B. Ghahreman, “Coalescence of fractures under shear stresses in experiments”, *J. Geophys. Res.* **100**:B4 (1995), 5975–5990.
- [Sibson 1985] R. H. Sibson, “Stopping of earthquake ruptures at dilational fault jogs”, *Nature* **316** (1985), 248–251.
- [Strayer and Hudleston 1997] L. M. Strayer and P. J. Hudleston, “Numerical modeling of fold initiation at thrust ramps”, *J. Struct. Geol.* **19**:3–4 (1997), 551–566.
- [Tang and Kou 1998] C. A. Tang and S. Q. Kou, “Crack propagation and coalescence in brittle materials under compression”, *Eng. Fract. Mech.* **61**:3–4 (1998), 311–324.
- [Thomas and Pollard 1993] A. L. Thomas and D. D. Pollard, “The geometry of echelon fractures in rock: implications from laboratory and numerical experiments”, *J. Struct. Geol.* **15**:3–5 (1993), 323–334.
- [Wang 2005] X. B. Wang, “Joint inclination effect on strength, stress-strain curve and strain localization of rock in plane strain compression”, *Mater. Sci. Forum* **495–497** (2005), 69–76.

- [Wang 2007a] X. B. Wang, “Effects of joint width on strength, stress-strain curve and strain localization of rock mass in uniaxial plane strain compression”, *Key Eng. Mater.* **353–358** (2007), 1129–1132.
- [Wang 2007b] X. B. Wang, “Failure process and stress-strain curve of plane strain rock specimen with initially random material imperfections”, *Key Eng. Mater.* **353–358** (2007), 1133–1136.
- [Wang 2007c] X. B. Wang, “Prediction of height effect, plastic deformation and fracture energy for high-strength concrete by linear shear softening constitutive relation based on energy conservation method”, *Mag. Concr. Res.* **59:5** (2007), 341–350.
- [Wang 2008] X.-B. Wang, “Influence of imperfection number on acoustic emissions and elastic strain energy decrease of rock specimens with initially random imperfections”, *Chin. J. Nonferr. Met.* **18:8** (2008), 1541–1549. In Chinese.
- [Wang and Pan 2008] X.-B. Wang and Y.-S. Pan, “Preliminary failure process modeling of strain-softening rocks with heterogeneity and stiffness deterioration”, pp. 767–771 in *Proceedings of the 3rd International Symposium on Modern Mining and Safety Technology* (Fuxin, 2008), Coal Industry Publishing House, Beijing, 2008.
- [Wang and Zhang 2009] X.-B. Wang and J. Zhang, “Numerical simulation of failure process of three-point bending concrete beam considering heterogeneity of tensile strength and post-peak softening curve”, *Eng. Mech.* **26:12** (2009), 155–160. In Chinese.
- [Wang et al. 2009] X.-B. Wang, D. Wu, F.-C. Zhao, and Y.-S. Pan, “Simulation of failure processes, precursors and overall deformation of rock specimens with different numbers of initially random imperfections”, *Prog. Geophys.* **24:5** (2009), 1874–1881. In Chinese.
- [Wawersik and Fairhurst 1970] W. R. Wawersik and C. Fairhurst, “A study of brittle rock fracture in laboratory compression experiments”, *Int. J. Rock Mech. Min.* **7:5** (1970), 561–575.
- [Zachariassen and Sieh 1995] J. Zachariassen and K. Sieh, “The transfer of slip between two en echelon strike-slip faults: a case study from the 1992 Landers earthquake, southern California”, *J. Geophys. Res.* **100:B8** (1995), 15281–15301.

Received 22 Jul 2010. Revised 13 Oct 2010. Accepted 14 Oct 2010.

XUE-BIN WANG: wxbbb@263.net

State Key Laboratory of Earthquake Dynamics, Institute of Geology, China Earthquake Administration, Beijing, 100029, China

and

College of Mechanics and Engineering, Liaoning Technical University, Fuxin, 123000, China

JIN MA: majin@ies.ac.cn

State Key Laboratory of Earthquake Dynamics, Institute of Geology, China Earthquake Administration, Beijing, 100029, China

LI-QIANG LIU: liulq-sohu@sohu.com

State Key Laboratory of Earthquake Dynamics, Institute of Geology, China Earthquake Administration, Beijing, 100029, China

JOURNAL OF MECHANICS OF MATERIALS AND STRUCTURES

<http://www.jomms.org>

Founded by Charles R. Steele and Marie-Louise Steele

EDITORS

CHARLES R. STEELE Stanford University, U.S.A.
DAVIDE BIGONI University of Trento, Italy
IWONA JASIUK University of Illinois at Urbana-Champaign, U.S.A.
YASUhide SHINDO Tohoku University, Japan

EDITORIAL BOARD

H. D. BUI École Polytechnique, France
J. P. CARTER University of Sydney, Australia
R. M. CHRISTENSEN Stanford University, U.S.A.
G. M. L. GLADWELL University of Waterloo, Canada
D. H. HODGES Georgia Institute of Technology, U.S.A.
J. HUTCHINSON Harvard University, U.S.A.
C. HWU National Cheng Kung University, R.O. China
B. L. KARIHALOO University of Wales, U.K.
Y. Y. KIM Seoul National University, Republic of Korea
Z. MROZ Academy of Science, Poland
D. PAMPLONA Universidade Católica do Rio de Janeiro, Brazil
M. B. RUBIN Technion, Haifa, Israel
A. N. SHUPIKOV Ukrainian Academy of Sciences, Ukraine
T. TARNAI University Budapest, Hungary
F. Y. M. WAN University of California, Irvine, U.S.A.
P. WRIGGERS Universität Hannover, Germany
W. YANG Tsinghua University, P.R. China
F. ZIEGLER Technische Universität Wien, Austria

PRODUCTION

PAULO NEY DE SOUZA Production Manager
SHEILA NEWBERY Senior Production Editor
SILVIO LEVY Scientific Editor

Cover design: Alex Scorpan


Cover photo: Ev Shafir

See inside back cover or <http://www.jomms.org> for submission guidelines.

JoMMS (ISSN 1559-3959) is published in 10 issues a year. The subscription price for 2010 is US \$500/year for the electronic version, and \$660/year (+\$60 shipping outside the US) for print and electronic. Subscriptions, requests for back issues, and changes of address should be sent to Mathematical Sciences Publishers, Department of Mathematics, University of California, Berkeley, CA 94720-3840.

JoMMS peer-review and production is managed by EditFLOW™ from Mathematical Sciences Publishers.

PUBLISHED BY

 **mathematical sciences publishers**
<http://www.mathscipub.org>

A NON-PROFIT CORPORATION

Typeset in L^AT_EX

©Copyright 2010. Journal of Mechanics of Materials and Structures. All rights reserved.

A semianalytical solution for the bending of clamped laminated doubly curved or spherical panels	
KASRA BIGDELI and MOHAMMAD MOHAMMADI AGHDAM	855
Analytical solution for a concentrated force on the free surface of a coated material	
ZHIGEN WU, YIHUA LIU, CHUNXIAO ZHAN and MEIQIN WANG	875
On the nonlinear dynamics of oval cylindrical shells	
S. M. IBRAHIM, B. P. PATEL and Y. NATH	887
Time-harmonic elastodynamic Green's function for the half-plane modeled by a restricted inhomogeneity of quadratic type	
TSVIATKO V. RANGELOV and GEORGE D. MANOLIS	909
An enhanced asymptotic expansion for the stability of nonlinear elastic structures	
CLAUS DENCKER CHRISTENSEN and ESBEN BYSKOV	925
Stress and strain recovery for the in-plane deformation of an isotropic tapered strip-beam	
DEWEY H. HODGES, ANURAG RAJAGOPAL, JIMMY C. HO and WENBIN YU	963
Assessment of the performance of uniform monolithic plates subjected to impulsive loads	
JONAS DAHL	977
Stress smoothing holes in planar elastic domains	
SHMUEL VIGDERGAUZ	987
Numerical simulation of failed zone propagation process and anomalies related to the released energy during a compressive jog intersection	
XUE-BIN WANG, JIN MA and LI-QIANG LIU	1007